Simulation of Interfacial Waves in Core-Annular Pipe Flow With a Turbulent Annulus

Li, Haoyu; Pourquié, Mathieu; Ooms, Gijs; Henkes, Ruud

DOI
10.1115/1.4066481

Publication date
2025

Document Version
Final published version

Published in
Journal of Fluids Engineering

ASME Journal of Fluids Engineering
Online journal at:
https://asmedigitalcollection.asme.org/fluidsengineering

Haoyu Li
Faculty of Mechanical Engineering,
Delft University of Technology,
Delft 2628 CD, The Netherlands
e-mail: eroujiqierji@gmail.com

Mathieu Pourquié
Faculty of Mechanical Engineering,
Delft University of Technology,
Delft 2628 CD, The Netherlands
e-mail: M.J.B.M.Pourquie@tudelft.nl

Gijs Ooms
Faculty of Mechanical Engineering,
Delft University of Technology,
Delft 2628 CD, The Netherlands
e-mail: Prof.Ooms@gmail.com

Ruud Henkes[1]
Faculty of Mechanical Engineering,
Delft University of Technology,
Delft 2628 CD, The Netherlands
e-mail: R.A.W.M.Henkes@tudelft.nl

Simulation of Interfacial Waves in Core-Annular Pipe Flow With a Turbulent Annulus

Numerical simulations are conducted for the wave initiation, growth, and saturation at the oil–water interface in core-annular flow (CAF). The focus is on conditions with a turbulent water annulus, but the laminar water annulus is also considered. The simulation results are compared with lab measurements. The growth rate for the linear instability of different wavelengths in the case of a turbulent water annulus is obtained from two-dimensional (2D) axisymmetric Reynolds-averaged Navier–Stokes (RANS) simulations with the Launder–Sharma low-Reynolds number k–ε model. The latter simulation results provide the most unstable wavelength for the turbulent water annulus. Our study also shows the following. The maximum wave growth rate for a turbulent water annulus is significantly higher than for a laminar water annulus. The most unstable wavelength in the simulations is about 25% smaller than in the experiments. The wave amplitude for the different wavelengths in the simulations is typically 17% lower than in the experiments.
[DOI: 10.1115/1.4066481]

Keywords: core-annular flow, interfacial waves, liquid–liquid interface instability

1 Introduction

Under certain conditions for two-phase liquid–liquid flow in a pipe, the less viscous liquid (e.g., water) can migrate to the high shear region near to the pipe wall (forming an annulus flow), leaving the more viscous liquid (like oil) in the center of the pipe (forming core flow). This flow pattern is referred to as core-annular flow (CAF); see the review by Joseph et al. [1]. In CAF, the less viscous liquid functions as a lubrication layer, which greatly reduces the pressure drop compared to the case in which only the high viscous liquid is transported through the pipe. Core-annular flow can be applied in the petroleum and chemical industry for effective transportation. This flow type is also of high interest for the understanding of the physics of interfacial waves in fluid mechanics.

Core-annular flow with a completely flat liquid–liquid interface is called perfect core-annular flow (PCAF). This CAF flow type is only possible in a vertical pipe for a small range of velocities, as visualized in the experiments by Chen et al. [2] and Yih [3]. In most practical cases, however, the flat interface cannot remain stable, and waves will develop leading to wavy core-annular flow (WCAF). In horizontal pipes, the presence of interfacial waves is essential to provide a downward force to balance the upward buoyancy force.

The formation of interfacial waves is caused by the instability of disturbances at the initially flat liquid–liquid interface of the flow. Over the years, the linear instability problem of laminar–laminar two-phase flow has been studied by various researchers. In the theoretical investigation of linear instability, the governing equations are linearized to describe a small disturbance with its growth rate. The solution is obtained by solving an eigenvalue problem for the linearized equation. The disturbance can be assumed to be a wave with a long, medium, or short length. Parameters that determine the linear instability include inertia, surface tension, viscosity, and gravity. Yih [3] shows that in two-dimensional (2D) liquid–liquid channel flow, a long wave instability exists for all values of the Reynolds number, and the instability is due to the viscosity difference between the two fluids. Hooper [4] studies the instability for two-phase plane Couette flow and finds that the flow is always unstable if the thickness of the layer with less viscous fluid is small. Hickox [5] finds that long waves are always unstable for an axisymmetric Poiseuille flow with the less viscous fluid in the core. Ooms [6] analyses the stability of laminar–laminar core-annular flow, while ignoring the effect of viscosity on the flow stability. He finds two types of instability: one is the Kelvin–Helmholtz instability, which is due to the apparent difference in flow velocity near the interface, and the other is a capillary instability, induced by the surface tension. The considered disturbance is axisymmetric and has a wavelength larger than the circumference of the oil core. Hooper and Boyd [7] study the short-wave instability of two viscous fluids in unbounded Couette flow. The flow is always unstable when surface tension is neglected. The instability is of a viscous nature and is created quickly close to the interface in the less viscous fluid part. Surface tension can stabilize this type of short-wave instability. Preziosi et al. [8] find that surface tension stabilizes short waves in core-annular flow. Long waves are destabilizing the flow and will lead to oil droplets in the water annulus. With increasing Reynolds number, the long wave capillary instability can be stabilized by shear. However, when the Reynolds number is above a critical value, a second capillary instability causes emulsion of oil into water. Therefore, upper and lower branches of the critical Reynolds number exist in relation to the neutral stability curve. This stabilization phenomenon agrees well with the experiment from Charles et al. [9].

Hu and Joseph [10] use the energy equation to study the linear instability mechanism for various parameters related to inertia,

[1]Corresponding author.

Contributed by the Fluids Engineering Division of ASME for publication in the Journal of Fluids Engineering. Manuscript received May 11, 2024; final manuscript received August 20, 2024; published online September 30, 2024. Editor: Francine Battaglia.

surface tension, interface stress, and wave Reynolds stress. At small Reynolds numbers, surface tension can cause instability, while the other two sources stabilize the flow. At large Reynolds number, surface tension stabilizes the flow, and the other two sources destabilize the flow. For even higher Reynolds number, the wave Reynolds stress in the water is the main source of instability. The wavy core-annular flow pattern in the experiment by Charles et al. [9] is regarded as a stable flow, in which the destabilizing Reynolds stress and the stabilizing interface viscosity compensate each other. Bai et al. [11] find a new flow pattern with bamboo waves in their vertical pipe flow experiment. Energy budgets show that the bamboo wave is induced by interfacial viscous friction, the surface tension is only slightly destabilizing, and the wave Reynolds stress stabilizes the flow. Miesen et al. [12] focus their analysis on disturbances with an intermediate wavelength. A rather good agreement is found when comparing the wave stability relationship with the experimental wave distribution. Boomkamp and Miesen [13] find five instability types for two-phase parallel flow. They argue that stable core-annular flow, as found in the stability analyses by Charles et al. [9], Hu and Joseph [10], and Miesen et al. [12], is due to the stabilizing effect of the presence of the jump in viscosity near the interface. When the wave amplitude becomes significant, nonlinear effects can saturate the linear instability. Papageorgiou et al. [14] study the nonlinear stability of CAF under the assumption that the annulus thickness is much smaller than the core radius.

Besides the linear and nonlinear theoretical analysis (using an eigenvalue approach), numerical simulations can also be used to study instability problems. Li and Renardy [15] use the volume-of-fluid (VOF) method to determine the instability in 2D vertical core-annular flow. Both the linear and nonlinear stages are simulated. Beerens et al. [16] also use the VOF numerical method. They verify the stable and unstable regions with the neutral curve from the theoretical analysis by Hu and Joseph [10]. They also reproduce the linear growth rate found in the theoretical analysis by Li and Renardy [15].

All the stability analyses referred to above consider a laminar–laminar two-phase base flow. In many applications, however, the base flow pattern can be turbulent. The presence of turbulence makes the stability problem even more challenging. Kuru et al. [17] and Náraigh et al. [18] carry out a linear stability analysis with a turbulent base flow in a stratified two-phase channel configuration. They use the quasi-static assumption; this means that the size of the turbulent fluctuations in space and time is much smaller than the magnitude of the mean velocity profile. The simulation results obtained in these two studies show that it is possible to split turbulence and waves. By doing so, the turbulent velocity profiles can be used as base state to determine physical instabilities with wave formation. It is found that the primary effect of turbulence is caused by the different average velocity profile for a turbulent flow when compared to the average velocity profile for a laminar flow.

The present study is focusing on the linear and nonlinear wave growth in core-annular flow, with a laminar oil core and a turbulent water annulus. We carry out a numerical analysis to track the full process of wave initiation, wave growth, and wave saturation. The simulation results are compared with experiments obtained in our lab. The work builds on recent core-annular flow studies by the same authors, Li et al. [19,20]. The simulation model consists of the Reynolds-averaged Navier–Stokes (RANS) equations with the Launder–Sharma low-Reynolds number k–ε model. This is a rather engineering approach to the wave growth problem, as it is not based on theoretical analysis with an eigenvalue analysis; we are just solving the flow equations and tracking the wave evolution. Our simulation approach is an extension to turbulent base flows compared to a similar laminar analysis carried out by Li and Renardy [15].

2 Experimental Setup

The flow loop (with a diameter of 21 mm) is approximately seven and a halve meter long and is made mostly of poly vinyl chloride. The measurement section is 3 m long and is made of plexiglas (PMMA) to enable flow visualization. In the divider, oil and water are added together. The oil is added through a concentric pipe within the pipe of the flow loop. In the annulus surrounding this pipe, the water is added in order to create core-annular flow. LabVIEW by national instruments is used to monitor the experiments and collect and process the data from pressure gauges and flow meters in the setup. Details on the flow loop and the applied measurement and flow visualization techniques are given by Vrijlandt [21].

The main purpose of this experiment is to measure the time-dependent film thickness of the water annulus. This is done by visualizing a part of the flow loop. The camera used for this visualization is a Phantom Vision VEO 640 L. To decrease the amount of optical distortion, an optical box is attached to the measurement section as shown in Fig. 1(*a*). A light emitting diode panel is placed behind the optical box to illuminate the measurement section so that clear images are produced. An example of a recorded image of the oil and water is shown in Fig. 1(*b*).

Because the light has to go through several media, the light is being refracted at each intersection. Since the height of the water film at the bottom is in the order of a millimeter, it is important to account for this distortion of the image. A simulation of the light beams coming from within the pipe to the position of the camera was made from which an optical distortion is acquired. To verify this ray-

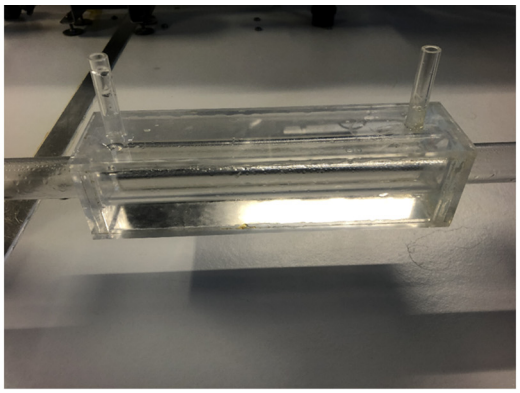

(*a*)

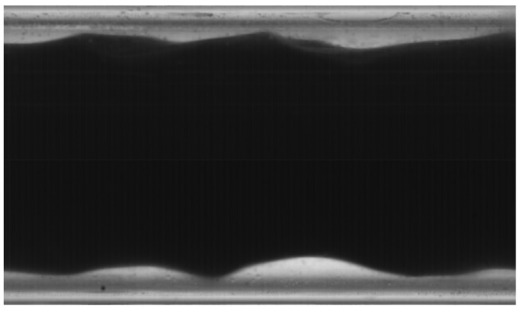

(*b*)

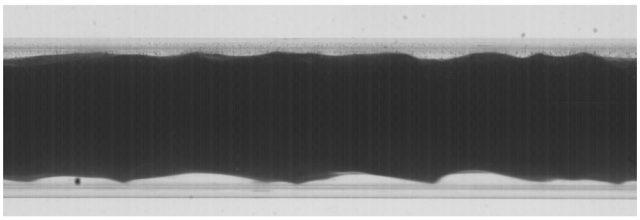

(*c*)

Fig. 1 Flow loop for core-annular flow experiments: (*a*) measurement section with optical box, (*b*) snapshot of recorded oil–water flow at 20% watercut, and (*c*) snapshot of recorded oil–water flow at 12% watercut

tracing method, a calibration pipe was made to make images of the pipe with a calibration piece. A measurement error of 0.01 mm is found, which is roughly 1% of the total film height.

3 Modeling Approach

The mass and momentum conservation equations for an incompressible, isothermal fluid read (in Cartesian coordinates)

$$\frac{\partial u_i}{\partial x_i} = 0 \tag{1}$$

$$\rho\frac{\partial u_i}{\partial t} + \rho u_j\frac{\partial u_i}{\partial x_j} = \frac{\partial}{\partial x_j}\left(\rho(\nu+\nu_t)\left(\frac{\partial u_i}{\partial x_j}+\frac{\partial u_j}{\partial x_i}\right)\right) - \frac{\partial p}{\partial x_i} + \rho g_i + F_{\sigma,i} \tag{2}$$

These are the RANS equations. Here, u_i is the velocity, ρ and ν are the fluid density and kinematic viscosity, g_i is the gravitational acceleration, p is the pressure, and $F_{\sigma,i}$ is the specific interfacial tension force. For the pipe flow, we use $x_1 = x$ for the coordinate along the pipe axis, and $x_2 = y$ and $x_3 = z$ for the coordinates in the cross-sectional plane; the velocity components are u, v, and w, in the directions x, y, and z, respectively. The gravity components are $g_1 = -g$ and $g_2 = g_3 = 0$, where g is the gravitational acceleration. The actual simulations are conducted using 2D axisymmetric coordinates with the radius $r = \sqrt{y^2+z^2}$.

The turbulent viscosity is modeled with the low-Reynolds number $k-\epsilon$ model of Launder and Sharma [22], which reads

$$\nu_t = C_\mu f_\mu \frac{k^2}{\tilde{\varepsilon}} \tag{3}$$

$$\frac{\partial k}{\partial t} + u_j\frac{\partial k}{\partial x_j} = \frac{\partial}{\partial x_j}\left(\nu+\frac{\nu_t}{\sigma_k}\right)\frac{\partial k}{\partial x_j} + \nu_t\left(\frac{\partial u_j}{\partial x_j}\right)^2 - \tilde{\varepsilon} - D \tag{4}$$

$$\frac{\partial \tilde{\varepsilon}}{\partial t} + u_j\frac{\partial \tilde{\varepsilon}}{\partial x_j} = \frac{\partial}{\partial x_j}\left(\nu+\frac{\nu_t}{\sigma_\varepsilon}\right)\frac{\partial \tilde{\varepsilon}}{\partial x_j} + C_1 f_1 \frac{\tilde{\varepsilon}}{k}\nu_t\left(\frac{\partial u_j}{\partial x_j}\right)^2 - C_2 f_2 \frac{\tilde{\varepsilon}^2}{k} + E \tag{5}$$

with $D = 2\nu(\partial\sqrt{k}/\partial x_j)(\partial\sqrt{k}/\partial x_j)$ and $E = 2\nu\nu_t(\partial^2 u_j/\partial x_j^2)^2$. The turbulent energy dissipation rate is $\varepsilon = \tilde{\varepsilon} + D$. Furthermore, $C_\mu = 0.09$, $C_1 = 1.44$, $C_2 = 1.92$, $\sigma_k = 1.0$, $\sigma_\varepsilon = 1.3$, $f_\mu = \exp(-3.4/(1+(\mathrm{Re}_t/50))^2)$, $f_1 = 1$, $f_2 = 1 - 0.3\exp(-\mathrm{Re}_t^2)$, and $\mathrm{Re}_t = k^2/\tilde{\varepsilon}\nu$. The boundary conditions at the wall are $k = 0$ and $\tilde{\epsilon} = 0$. Quite a few low-Reynolds number $k-\epsilon$ formulations are available in the literature. A large advantage of using the Launder–Sharma one is that the low-Reynolds number terms do not include the explicit distance to the closest wall. Instead, the parameter Re_t is used to incorporate the effect of turbulence damping when a wall is approached. In the same way, the model will incorporate the possible damping of turbulence when the oil–water interface is approached in core-annular flow. The low-Reynolds number $k-\epsilon$ model is used everywhere in the domain, also in the laminar oil core. Because of the presence of the low-Reynolds number terms, the model automatically relaminarizes in the viscous oil core (i.e., it gives zero turbulent viscosity).

We use the open-source package OPENFOAM to solve the RANS equations, applying the coupled level set VOF (CLSVOF) method for the interface capturing. The CLSVOF solver is based on the interFoam VOF solver in OPENFOAM. In the CLSVOF solver, the level set function is used to calculate the interfacial tension force. Starting from the VOF method, the volume fraction α is introduced to distinguish between the two fluid phases: $\alpha = 0$ is the oil phase, $\alpha = 1$ is the water phase, and $0 < \alpha < 1$ denotes the oil–water interface. Then, the fluid density and viscosity in the equations are

$$\rho = (1-\alpha)\rho_o + \alpha\rho_w \quad \text{and} \quad \mu = (1-\alpha)\mu_o + \alpha\mu_w \tag{6}$$

The subscript "o" refers to oil, and the subscript "w" refers to water. α is calculated from the following advection equation:

$$\frac{\partial \alpha}{\partial t} + \nabla\cdot(\alpha\mathbf{u}) + \nabla\cdot((1-\alpha)\alpha\mathbf{u}_r) = 0 \tag{7}$$

The third term on the left-hand side is the compressive term (with the divergence of the compressive flux); here, $\mathbf{u}_r = \mathbf{u}_w - \mathbf{u}_o$. This term is devised to control the sharpness of interface.

The level set function Φ is defined as the distance from the interface, where the interface is the isoline with $\Phi = 0$. The initial value of the level set function Φ_o is obtained from the initialized volume-of-fluid field, where the interface is defined at $\alpha = 0.5$

$$\Phi_0 = (2\alpha - 1)\Gamma \tag{8}$$

$$\Gamma = 0.75\Delta X \tag{9}$$

Here, ΔX is the minimum mesh size near the interface. Thereafter, the re-initialization equation is solved to turn the initial level set function into the distance from the interface

$$\frac{\partial \Phi}{\partial \tau} = \mathrm{sign}(\Phi_0)(1 - |\nabla\Phi|) \tag{10}$$

Here, τ is a pseudotime, with $\Delta\tau = 0.1\Delta X$ being the iteration time-step of Φ. The sign function denotes

$$\mathrm{sign}(\Phi) = \begin{cases} 1 & \Phi > 0,\ water \\ 0 & \Phi = 0,\ interface \\ -1 & \Phi < 0,\ oil \end{cases} \tag{11}$$

Then, the interface tension force is calculated as

$$\mathbf{F}_\sigma = \sigma\kappa(\Phi)\delta_\Phi\nabla(\Phi) \tag{12}$$

Here, σ is the interface tension, and δ_Φ is the smoothed delta function

$$\delta_\Phi = \begin{cases} \frac{1}{2\gamma}\left(1+\cos\left(\frac{\pi\Phi}{\gamma}\right)\right) & \text{for } |\Phi| < \varepsilon \\ 0 & \text{elsewhere} \end{cases} \tag{13}$$

The quantity γ is the interface thickness coefficient (see Ref. [23]), and $\kappa(\Phi)$ is the interface curvature

$$\kappa(\Phi) = \nabla\cdot\mathbf{n}_c \tag{14}$$

$$\mathbf{n}_c = \frac{(\nabla\Phi)_f}{|(\nabla\Phi)_f|} \tag{15}$$

Here, $\mathbf{n}_c$ is the surface unit normal vector. The contact angle θ between the interface and the pipe wall is defined as

$$\cos(\theta) = \mathbf{n}_c\cdot\mathbf{n}_w \tag{16}$$

with $\mathbf{n}_w$ being the unit normal vector at the wall. The contact angle is set to 90 deg in our simulations. This means that both the level set function Φ and the volume fraction of the fluid α satisfy the zero-gradient condition at the pipe wall boundary.

A pressure drop in the flow direction is added as an extra force term to the right-hand side of Eq. (2). In all the simulations, periodic boundary conditions are applied on the left and right sides of the pipe, which restricts the wavelengths to at most the considered domain length. At the pipe wall, the no-slip condition is imposed.

Four hydraulic parameters can be considered: the total flow rate, the pressure drop, the watercut, and the water holdup fraction. The watercut is defined as the ratio of the water volumetric flow rate and the total volumetric flowrate $\mathrm{WC} = Q_w/(Q_w+Q_o)$, where Q

denotes the volumetric flow rate. The water holdup fraction is defined as the ratio of the in situ water volume in the pipe and the total volume of oil and water $\alpha_w = V_w/(V_w + V_o)$. For a given configuration, when two out of the four parameters are set as input, the other two will follow from postprocessing of the results from the simulations or lab experiments. It is also convenient to introduce the holdup ratio, which is defined as $h = (Q_o/Q_w)/(V_o/V_w)$.

4 Wave Stability Curves

4.1 Vertical Laminar–Laminar Core-Annular Flow. Li and Renardy [15] consider the linear and nonlinear stability of laminar–laminar upward going core-annular flow. They are numerically solving the eigenvalue problem of the linearized Navier–Stokes equations (which is in fact the Orr–Sommerfeld equation) to determine the most unstable linear modes. Li and Renardy [15] refer to that solution as the one with "theoretical linear growth rate." In addition, they are numerically solving the Navier–Stokes equations to obtain both the linear and nonlinear wave growth. Thereto, the VOF numerical method is applied to the vertical laminar–laminar core-annular flow. When imposing a small initial disturbance on the flat liquid–liquid interface, the linear instability gives an exponential growth of the wave amplitude over time $A^*(t^*) = A^*(0)\exp(k^*t^*)$, where A^* is the wave amplitude, made dimensionless with the radius of the oil core (i.e., $A^* = A/R_c$), t^* is the time, made dimensionless with the centerline velocity and the oil core radius (i.e., $t^* = tR_c/U_c$), and k^* is the (dimensionless) growth rate.

To verify our numerical method, one of the laminar–laminar cases from Li and Renardy [15] for vertically upward going flow ($\vartheta = 90$ deg) is considered. The wave number is defined as $\gamma^* = 2\pi/\lambda^*$, with dimensionless wavelength $\lambda^* = \lambda/R_c$. Only the axisymmetric modes are simulated. We apply a 256×256 mesh in axial and radial direction (which is the same mesh as used by Li and Renardy); the mesh size is $\lambda/256$ in axial direction and the average mesh size is $R/256$ in radial direction (with pipe radius R). The initial velocity distribution is set according to the analytical expression of PCAF. Repeating the simulations on refined meshes shows that the results on the 256×256 are numerically accurate (details not included here). A more detailed mesh dependence description for a turbulent base flow is given in Sec. 4.2.

Figure 2 compares our results from the 2D axisymmetric simulation with the theoretical linear values of Li and Renardy [15]. Figure 2(*a*) shows a close agreement for the wave stability curve (i.e., growth rate versus wave number), in which the wave number $\gamma^* = 2$ marks the most (linearly) unstable wavelength. The numerical result for each wavelength in the figure was obtained from a simulation with periodic boundary conditions for a pipe section with the length of the considered wave. The growth rate is derived from the simulation results by assuming exponential growth in the time interval t^* between 1.5 and 3. The numerical values of the growth rate are quite close to the theoretical values. As shown in Fig. 2(*b*), the wave number $\gamma^* = 2$ initially gives a growth rate of $k^* = 0.20$ in the numerical simulations, which is close to the theoretical value of $k^* = 0.1940$, reported by Li and Renardy [15].

Because we only disturb the interface at time zero, while the velocity and pressure field will experience the disturbance once the effect of the wave growth has propagated, the flow system takes a brief time to enter the linear growth region; this can explain the small plateau near time zero. The linear growth is clearly visible until t^* is 10, after which, due to nonlinear effects, the growth levels off and reaches a saturation. A similar numerical procedure as used for laminar–laminar CAF is applied to laminar–turbulent CAF, as will be discussed in Sec. 4.2.

4.2 Laminar–Turbulent Core-Annular Flow. To study the instability of laminar–turbulent core-annular flow, we first perform a mesh sensitivity study for the growth rate. The selected conditions are the following (same as those used in our lab experiments for core-annular flow). The pipe radius is 10.5 mm, the oil density is

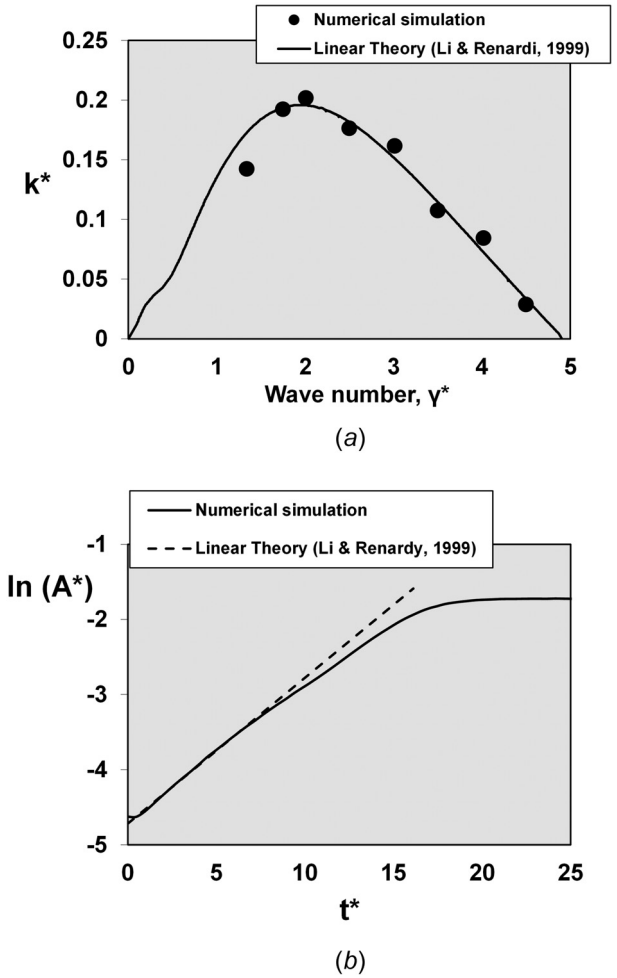

Fig. 2 Verification of numerical method against theoretical linear values from Li and Renardy for the instability of laminar–laminar core-annular flow: (*a*) wave stability curve and (*b*) growth of the dimensionless wave amplitude A^* for wave number $\gamma^* = 2$

$\rho_o = 902\ \text{kg/m}^3$, the water density is $\rho_w = 993\ \text{kg/m}^3$, the dynamic oil viscosity is $\mu_o = 0.697$ Pa·s, the dynamic water viscosity is $\mu_w = 6.65 \times 10^{-4}$ Pa·s, and the interfacial tension is $\sigma = 0.016$ N/m. The imposed total flow rate is $Q = 0.00043\ \text{m}^3/\text{s}$ (i.e., 1.24 m/s mixture velocity), and the imposed water holdup fraction is 0.26.

To initialize the flow, fully developed perfect core-annular flow (i.e., no interfacial waves), though with a turbulent water annulus, is first simulated in a pipe with very small streamwise section length. A strongly nonequidistant mesh is used in radial direction, giving a high concentration of points close to the pipe wall.

After obtaining the one-dimensional (1D) fully developed flow, the 1D result is mapped into a 2D domain with a certain length of the pipe section. In streamwise direction, the radial location of the interface is slightly disturbed with a sinusoidal shape with a wavelength equal to the length of the pipe section to trigger the possible wave growth over time. In this simulation example for CAF with a turbulent water annulus, the length of the pipe section is set to 9.6 mm, which corresponds to the dimensionless wavelength $\lambda^* = 1.06$ (being about the most unstable wave, as will be shown later). The simulations are repeated at successively refined grids: 75×200, 150×400, and 300×800 points in the streamwise $\times$ radial directions. A uniform mesh is used in streamwise direction; the mesh size is L/N (with L the section length and N the number of streamwise mesh cells). In radial direction, a nonuniform mesh is used: using a tanh-type stretching function, the mesh size is decreased when approaching the pipe wall. The average mesh size in

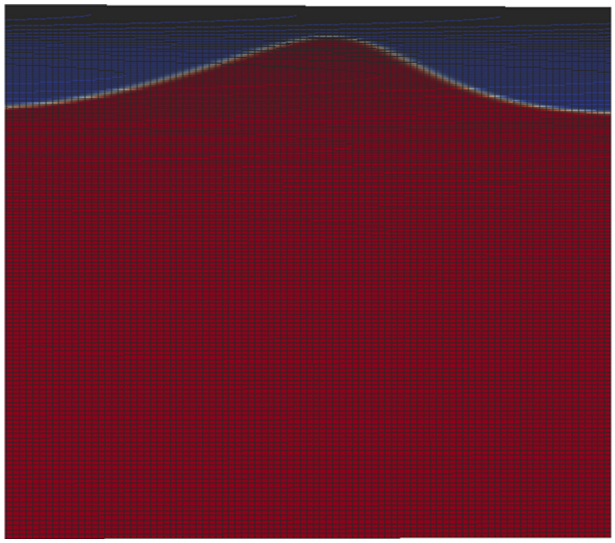

Fig. 3 Example simulation result with distribution of mesh points. Oil in lower layer and water in upper layer. Mesh point lines in black.

radial direction is R/M (with R the pipe radius and M the number of radial mesh cells). Figure 3 shows an example case for the interface wave between oil (lower layer) and water (upper layer) with a distribution of the mesh points (with black lines).

The simulation results are shown in Fig. 4(*a*). Like for the laminar–laminar case, also for this laminar–turbulent case, there is an initial linear phase with exponential growth of the wave amplitude over time. The results are almost mesh independent, with a linear growth rate close to $k^* = 0.65$, which is significantly higher than the value of 0.20 found for the laminar–laminar case in Sec. 4.1. The 150×400 mesh resolution is used for the further analysis of the nonlinear wave instability. The 75×200 mesh is used for a sensitivity study for the fully developed saturated waves.

The "quasi-laminar assumption" (as described by Náraigh et al. [18]) is also tested. This means that the 1D turbulent mean velocity profile is used as the initial condition, but that the 2D laminar Navier–Stokes equations are solved when monitoring the wave growth. As shown in Fig. 4(*b*), this is done for both a case in which the turbulent viscosity is set to zero in the dynamic simulation and for a case in which the turbulent viscosity remained fixed at its initial value. The figure shows that the simulation results for the three approaches initially give the same amplitude growth. Thereafter, the simulation with the quasi-laminar assumption gives a slower growth rate than the simulation that uses RANS with the $k - \varepsilon$ model for the turbulence in the water annulus over time. The close agreement for small time is due to the vanishing turbulence (i.e., laminar like profile) close to the interface.

The wave growth simulations are carried out for different lengths of the pipe section, with periodic boundary conditions (using the turbulence model). This provides the wave stability curve for the laminar–turbulent case (upper curve) that is shown in Fig. 5(*a*). The imposed water holdup fraction of 0.26 gives a watercut of 15% in the 1D initial flow (i.e., without waves). For large wave numbers (or small wavelengths), no wave growth is found. This confirms that the waves below a threshold value length cannot develop as they are damped through energy dissipation (e.g., viscous damping). For small wave numbers (or large wavelengths), two waves, instead of one unstable wave, are found. This is because the wave with half the length of the simulated section is more unstable (i.e., larger growth rate) than the wavelength that is equal to the length of the simulated section. Figure 5 only shows the simulations results with nonzero wave growth when a single wave is found.

Figure 5(*b*) shows the wave stability curves for different values of imposed water holdup fraction, while the imposed mixture velocity remained fixed at 1.24 m/s. The water annulus is turbulent for the

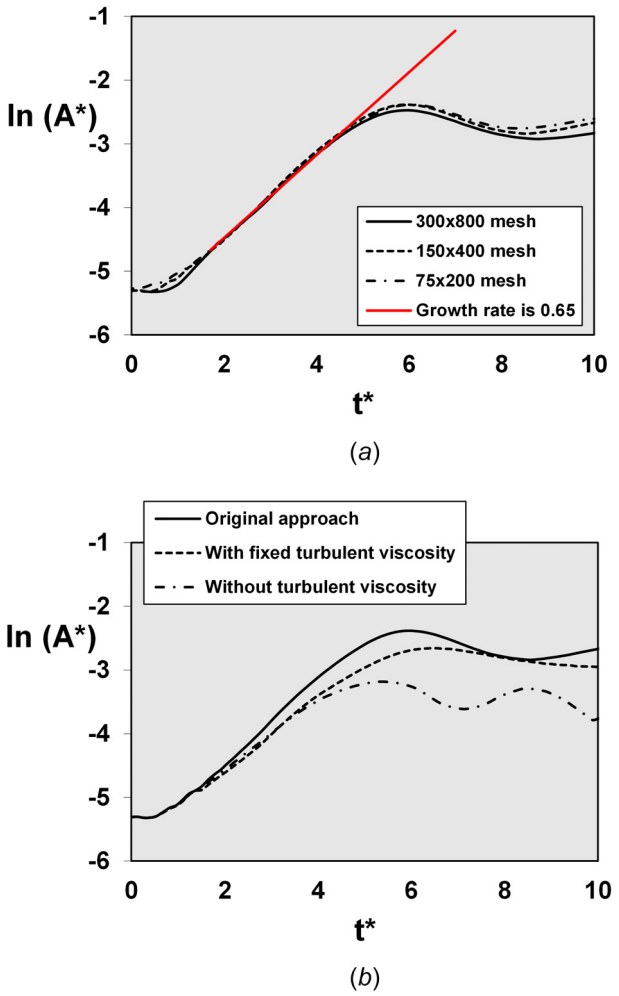

Fig. 4 Growth of the dimensionless wave amplitude A^* over dimensionless time t^* for the case with laminar–turbulent core-annular flow: (*a*) mesh sensitivity and (*b*) comparison of three approaches on a 150 × 400 mesh

water holdups fractions of 26%, 19%, and 14%, but a laminar water annulus is found if the water holdup fraction is decreased to 7%. All wave stability curves show a clear maximum, which identifies the most unstable wavelength, for a given water holdup fraction. The most unstable wavelengths (or wave numbers) are summarized in Table 1. A decrease in water holdup fraction gives a slight decrease in the most unstable wavelength (or increase in the most unstable wave number). When the water annulus becomes laminar (at 7% water holdup fraction), the most unstable wavelength decreases, and its growth rate is significantly smaller than for the turbulent water annulus (found at higher water holdup fractions).

The decrease in growth rate when going from a turbulent water annulus to a laminar water annulus is also observed when the water annulus at 26% water holdup fraction is relaminarized through increasing the water dynamic viscosity μ_w with a factor five (i.e., from 6.65×10^{-4} Pa·s to 33×10^{-4} Pa·s). Figure 5(*a*) shows that the growth rate for the most unstable wave decreases from 0.69 to 0.15 when the turbulent flow is forced to relaminarize through artificially increasing the water dynamic viscosity. This is in line with the physical intuition that more viscosity (or more viscous damping) makes it more difficult for waves to develop and grow.

5 Wave Growth Behavior

5.1 Flow Pattern During Unstable Stage. We have already shown that the initial formation of interfacial waves is due to a linear

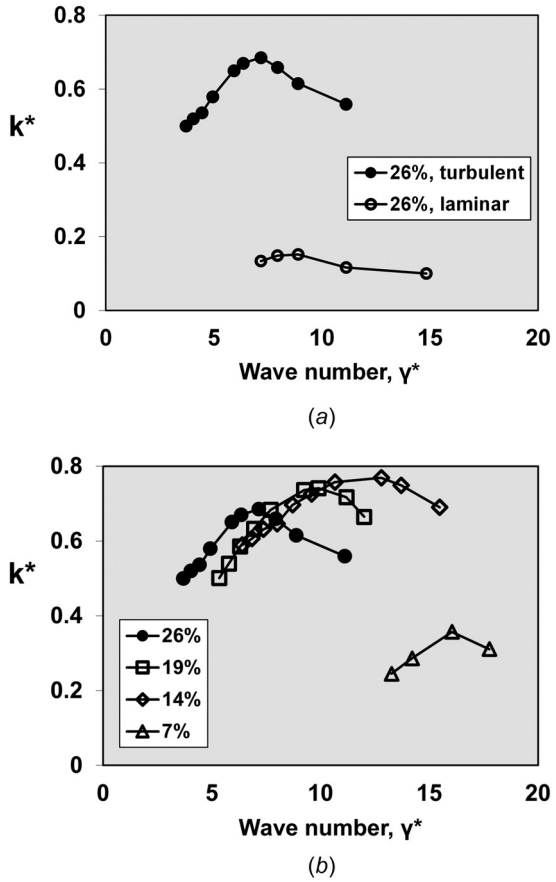

Fig. 5 Dimensionless linear wave growth rate k^* as a function of the wavenumber γ^*: (*a*) at 26% water holdup fraction for turbulent and laminar water annulus and (*b*) for different values of the imposed water holdup fraction with turbulent water annulus

Table 1 Most unstable wave for core-annular flow for different values of the water holdup fraction; wavelength (λ, λ^*), wave number (γ^*), and wave growth rate (k^*)

Water holdup (%)	λ (mm)	λ^*	γ^*	k^*
26	7.9	0.88	7.2	0.69
19	6	0.63	9.9	0.74
14	4.8	0.49	13	0.77
7	4	0.39	16	0.36

instability. Once the wave amplitude has become sufficiently large, nonlinear effects saturate the growth until a stable WCAF is obtained. Figure 6 shows the evolution from PCAF to WCAF for 26% imposed water holdup fraction and 1.24 m/s imposed mixture velocity, with a section length (or wavelength) of 9.6 mm ($\lambda^* = 1.06$). To better see the flow structure, two periodic waves are shown at different time levels (namely, $t^* = 3.4$, 5.5, 6.9, and 40). Referring to Fig. 6, shown are the isobars with streamlines in the left graphs, and the turbulent viscosity level in the rights graphs. The streamlines are shown with respect to a reference frame that moves with the wave velocity. Figure 7 shows the evolution of the dimensionless pressure drop (the Fanning friction factor), the turbulent viscosity, and the watercut. The Fanning friction factor is defined as the ratio of minus the streamwise pressure gradient and $\rho_w U_{\text{mix}}^2/R$.

During the linearly unstable stage (which takes up to about $t^* = 4$), the pressure drop (or Fanning friction factor), the maximum turbulent viscosity, and watercut (as shown in Fig. 7) change only little over time, although the wave amplitude grows exponentially. After the linear state, there is a relatively long nonlinear stage (between about $t^* = 4$ and 20). Thereafter, the saturated long-term stage is reached. In particular, the pressure drop increases from 425 Pa/m to 790 Pa/m (or the Fanning friction factor from 0.00293 to 0.0054), the watercut from 15% to 22%, and the maximum turbulent viscosity (ν_t/ν_w) from 10.8 to 16.7. As the water holdup remains constant at 26%, the corresponding holdup ratio decreases from 1.8 to 1.24.

Several phenomena can be observed in the streamlines, pressure level and turbulent viscosity level, as shown in the transients in Fig. 6 and the snapshots in Fig. 7. During the time interval in the linear stage (i.e., up to about $t^* = 4$), the wave amplitude grows exponentially, while an increasing recirculation zone develops behind the wave crest. In the nonlinear wave growth stage (i.e., between about $t^* = 4$ and 20), the wave amplitude continues to increase, and the recirculation region becomes larger and larger. At the top of the vortex in the recirculation zone, the streamwise velocity decreases, because of the high negative relative velocity in the reference frame of the interface. This causes some local laminar flow (see the right graph in Fig. 6(*b*)). The maximum turbulent viscosity shows only a small increase. The pressure drop is almost the same as in the 1D initial state. The low pressure behind the wave crest produces a negative pressure force (form drag) to decelerate the oil core and accelerate the water layer. As shown in Fig. 7(*c*), the watercut also increases during this stage.

After about $t^* = 7$ (going from the flow in Fig. 6(*c*) to Fig. 6(*d*)), under the effect of pressure, the interfacial wave changes its shape into one with a rather flat profile at the trough and a sharp profile at the crest. The vortex has gradually dissipated, which is in line with a smaller absolute value of the pressure. The recirculation zone also started to move to the left. During the dissipation of the vortex, the water layer becomes more turbulent, as shown from the sharp increase in the turbulent viscosity in Fig. 7(*b*). Then, pressure drop also increases rapidly. The turbulent viscosity decreases continuously after $t^* = 8$. The final (saturated nonlinear) state is reached at about $t^* = 40$.

5.2 Comparison with Saturated Wave Pattern in Experiments. Experiments are conducted in our lab for various watercuts with core-annular flow in a horizontal pipe with 21 mm diameter. See the flow loop description in Sec. 2. The base condition is a total flow rate of 0.00043 m^3/s (mixture velocity of 1.24 m/s) with 20% watercut. This gives a water holdup fraction of 0.26. Other watercuts are obtained by keeping the oil flow rate fixed at 0.00034 m^3/s (or superficial oil velocity of 0.8×1.24 m/s), and adding water until the watercut is 15% or 10%. The measured water holdup fractions for the latter are 0.21 and 0.16, respectively. It should be emphasized that these experiments do not include the controlled initiation of waves from an initially flat interface, but they only cover the fully developed flow with the saturated wave structure. At the inlet of the experimental pipe, oil is injected in the pipe center, and water is injected in the annulus location. The fully developed flow is monitored at the downstream location. Therefore, in contrast with the simulations, the experiments do not start with perfect core-annular flow (i.e., smooth interface).

From the experiments, the saturated interfacial waves are captured by a high-speed camera (pipe diameter is 21 mm, and the section length shown is 38 mm). The resolution is 100 pixels per mm, and the sampling rate is 1000 frames per second. Requiring at least four pixels and four frames, the spatial resolution is 0.04 mm, and the temporal resolution is 0.004 s. This enables to accurately track the waves, which have a dominant wavelength of about 10 mm, and a minimum length of about 2 mm, traveling with a velocity of about 1.3 m/s. The ray-tracing method is used to calibrate the recorded frames, meant to exclude the reflection effect of the pipe wall material and to fix the wall location. Sample raw images taken from the footage are shown in Fig. 1(*b*)/1(*c*) of Sec. 2.

The developed flow in the experiments is monitored over a time duration of 3 s, in which multiple wavelengths are captured by the camera. The duration of a wave is taken as the time between two subsequent maxima in the time signal at a certain fixed streamwise

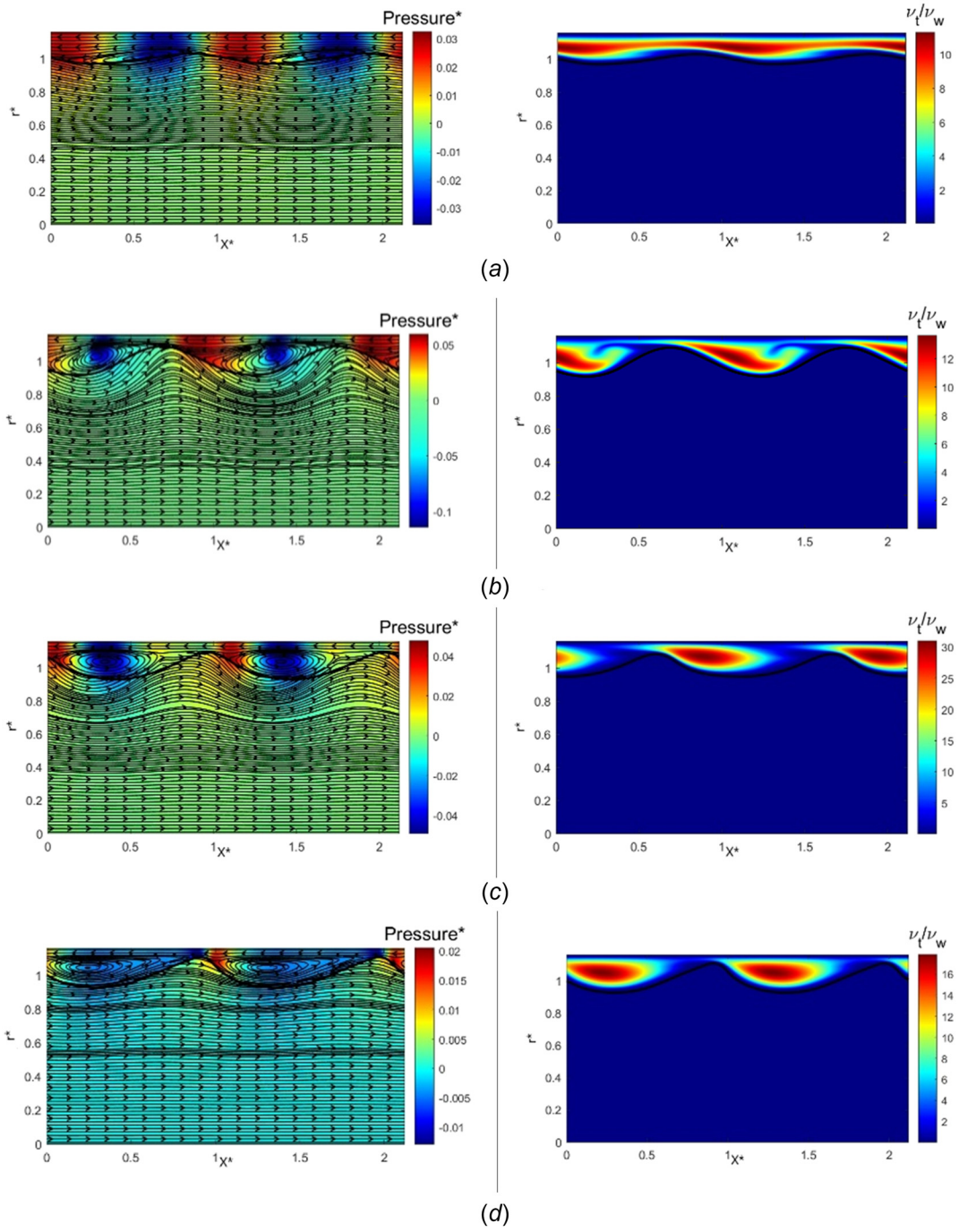

Fig. 6 Flow pattern during the unstable stage at different time levels (26% water holdup fraction, 1.24 m/s mixture velocity, 9.6 mm wavelength, $\lambda^* = 1.06$); (left) isobars with streamlines and (right) turbulent viscosity ratio level. (*a*) $t^* = 3.4$, (*b*) $t^* = 5.5$, (*c*) $t^* = 6.9$, and (*d*) $t^* = 40$.

location. The wave velocity is deduced through correlating the maxima in the recorded interface time traces at two slightly shifted streamwise locations. By using the measured wave velocity (which is about 1.37 m/s for the top layer and 1.21 m/s for the bottom layer, for the 26% water holdup fraction case, or 20% watercut case), the measured time period is converted to the wavelength. Figure 8 shows the wavelength distribution derived from the experiments. Thereto, all the detected wavelengths with their duration are distributed among wavelength intervals (ten equal intervals are used up to the maximum wavelength found). Thereafter, the total duration time of the waves that ended up in each interval is compared: this gives the pdf (probability density function) of the wavelength. The pdf is scaled such that the area under the curve showing the pdf versus the wavelength is equal to one. The wavelength distribution is rather broad; the spread in the waves at the top of the pipe is smaller than at the bottom of the pipe. The maximum denotes the most dominant wavelength. Almost the same value for this is found at the bottom and top (slightly longer at the bottom). Since a horizontal pipe is used in the experiment, gravity causes some eccentricity of the oil core with a thicker water annulus at the bottom than at the top. The thicker bottom water layer allows the waves to become longer with a larger amplitude. This is also clear in the experimental time-dependent evolution of the water annulus thickness, as shown for the 25% water holdup case and the 19% water holdup case in Fig. 9: the average thickness of the water annulus is larger in the bottom layer than in the top layer.

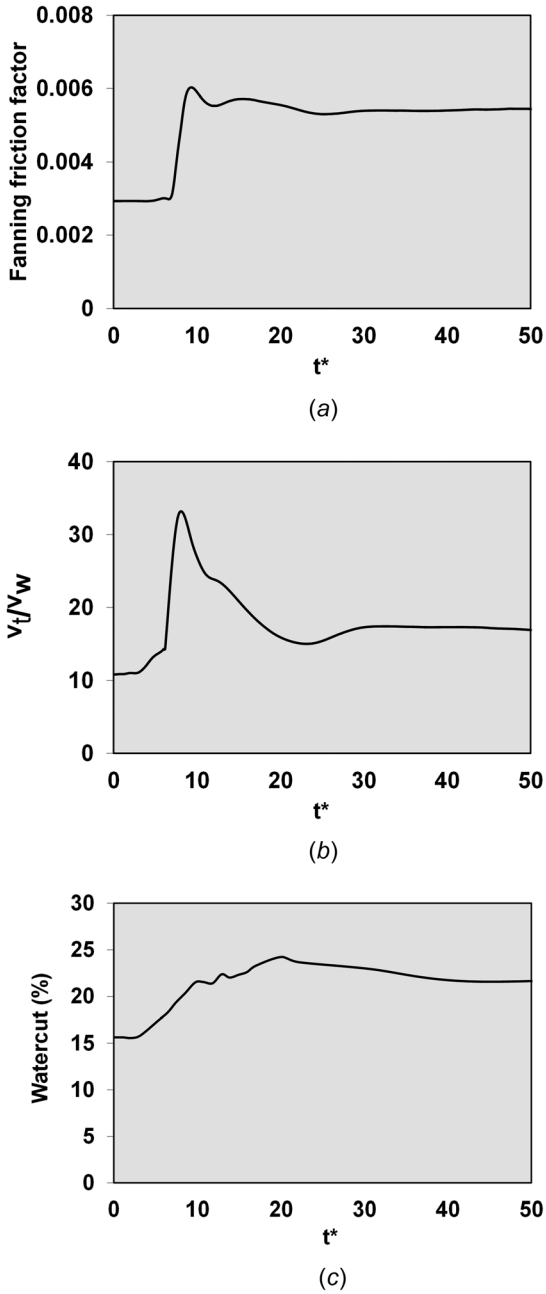

Fig. 7 Hydraulic parameters during the unstable stage (26% water holdup fraction, 1.24 m/s mixture velocity, 9.6 mm wavelength, $\lambda^* = 1.06$): (*a*) Fanning friction factor, (*b*) maximum in the turbulent viscosity ratio, and (*c*) watercut

Figure 8 also includes the wavelength distribution (in pdf form) as obtained from the 2D axisymmetric (i.e., concentric) simulation in a pipe with the same conditions as in the experiment, though with a finite length of 12 pipe diameters (using periodic boundary conditions). The simulated wavelength distribution is in fairly good agreement with the lab experiments: the dominant wavelength (i.e., the wavelength where the pdf is maximum) is about 25% smaller in the simulation than in the experiments.

The wavelength with the highest simulated growth rate corresponds to the dominant wavelength found in the simulation for the 12-diameter long pipe section. For an increasing water holdup fraction in the simulation, the dominant wavelength (i.e., the wavelength with the highest growth rate) in the simulations becomes longer. For the smaller water holdup fractions (14% and 19%), the most frequent wavelength is around 0.6 times the oil core radius ($\lambda^* = 0.6$), whereas for the larger water holdup fraction (26%), the

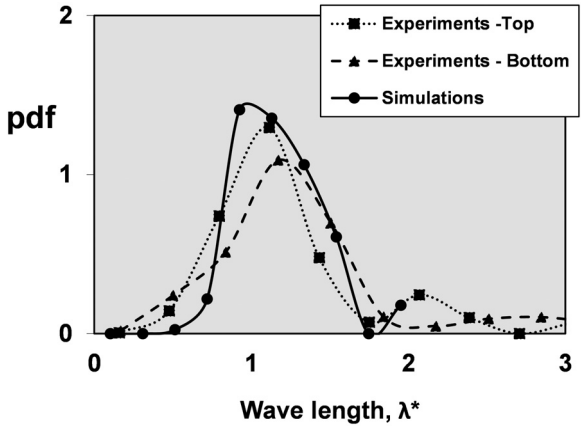

Fig. 8 Saturated wave distribution (pdf for λ^*) for 26% water holdup fraction

most frequent wavelength is almost equal to the oil core radius ($\lambda^* = 1$).

The values of the wavelengths in the simulation and in the experiments are compared in Table 2. The results for the numerical

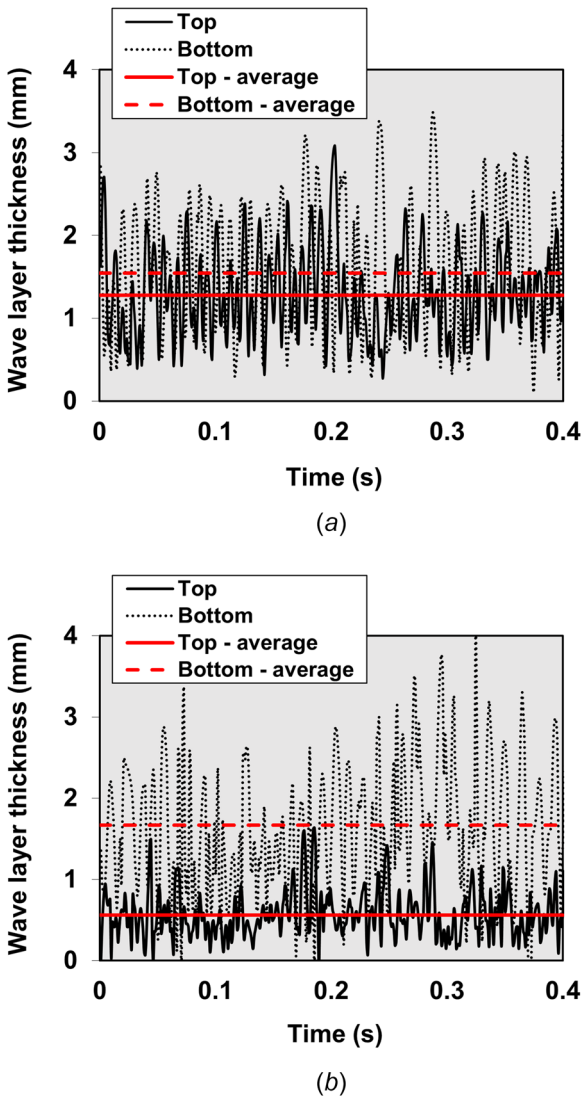

Fig. 9 Experimental time traces of the water annulus thickness: (*a*) 26% water holdup and (*b*) 19% water holdup fraction

Table 2 Minimum, maximum, and the most dominant dimensionless wavelength λ^* for the three considered cases

Water holdup fraction (%)	Wavelength λ^*	Numerical simulation	Experiment top layer	Experiment bottom layer
26	Minimum	0.5	0.2	0.3
	Maximum	1.8	1.9	2.2
	Dominant	0.9	1.1	1.2
	Eccentricity	0	0.12	
19	Minimum	0.4	0.2	0.2
	Maximum	1.2	1.9	2.2
	Dominant	0.6	0.7	0.9
	Eccentricity	0	0.5	
14	Minimum	0.4	0.2	0.2
	Maximum	1	1.9	2.2
	Dominant	0.6	0.7	0.9
	Eccentricity	0	0.47	

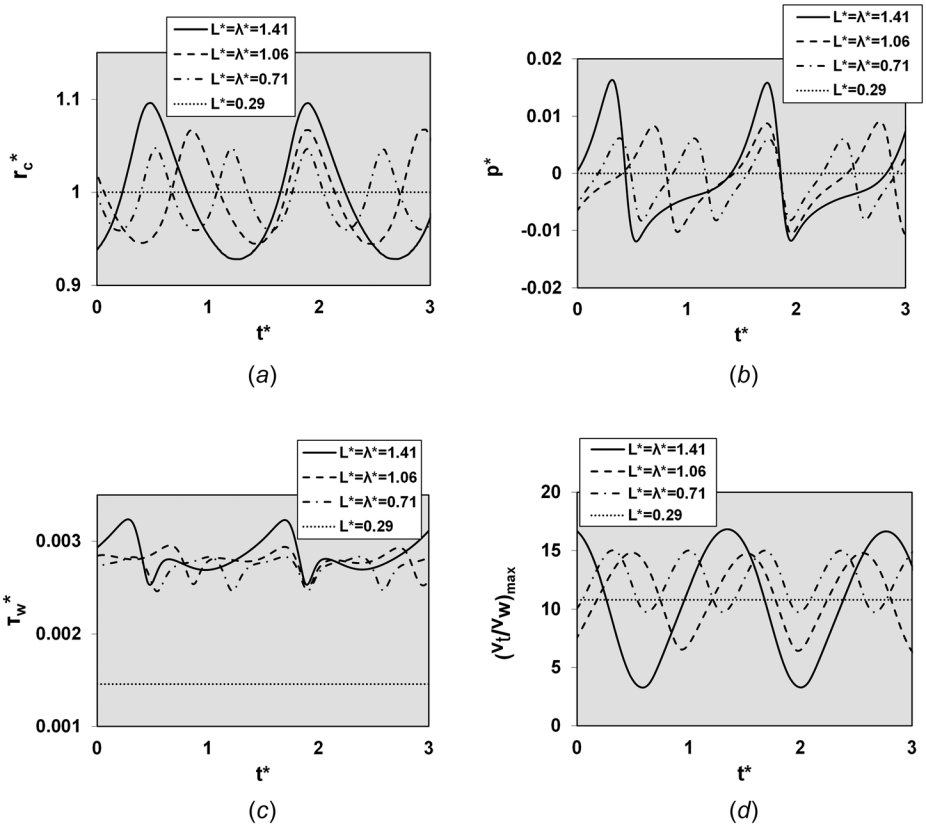

Fig. 10 Flow characteristics at a fixed axial location for fully developed flow in different pipe section lengths L^* in the simulations: (*a*) dimensionless interface location, (*b*) dimensionless wall pressure, (*c*) dimensionless wall shear stress, and (*d*) maximum in the turbulent viscosity ratio

simulations are based on results obtained for the growth of waves in pipe sections with a variety of lengths (using periodic boundary conditions); this allows to monitor the growth (or damping) of a single wavelength. The obtained range of stable waves is in fact reflected in the spectrum of waves found in the simulations for the much longer pipe section of 12 pipe diameter. This is shown in Fig. 8. A simulation can contain multiple traveling waves. According to Table 2, the smallest possible wavelength in the experiment is smaller than in the simulations. It should be noted that in the experiment, the oil core is somewhat eccentric toward the pipe top. In the numerical simulations, the flow is assumed to be 2D axisymmetric, giving a concentric oil core. This difference (eccentric versus concentric) can affect the stability behavior. Therefore, only a part of the wave stability relationship could be obtained in the simulations. The predicted 2D axisymmetric linear instability growth rate agrees well with the distribution of the longer wavelengths observed in the experiments. Table 2 also includes the eccentricity of the oil core in the measurements. The eccentricity is defined as $e = (d_{\text{bottom}} - d_{\text{top}})/(d_{\text{bottom}} + d_{\text{top}})$. Thus, $e = 0$ for a concentric oil core, and $e = 1$ for a fully eccentric oil core. Due to the effect of gravity on the horizontal flow, the experimental results reveal an eccentricity. As the simulation is axisymmetric, its eccentricity is zero.

5.3 Fully Developed Waves—Effect of Wavelength. As a range of wavelengths is observed in the experiment, the effect of the wavelength on the mean flow will be studied. Various pipe section lengths L are simulated sufficiently long over time until the flow has become fully developed. For the smaller section lengths, the wavelength is equal to the section length, i.e., $\lambda^* = L^*$. When the

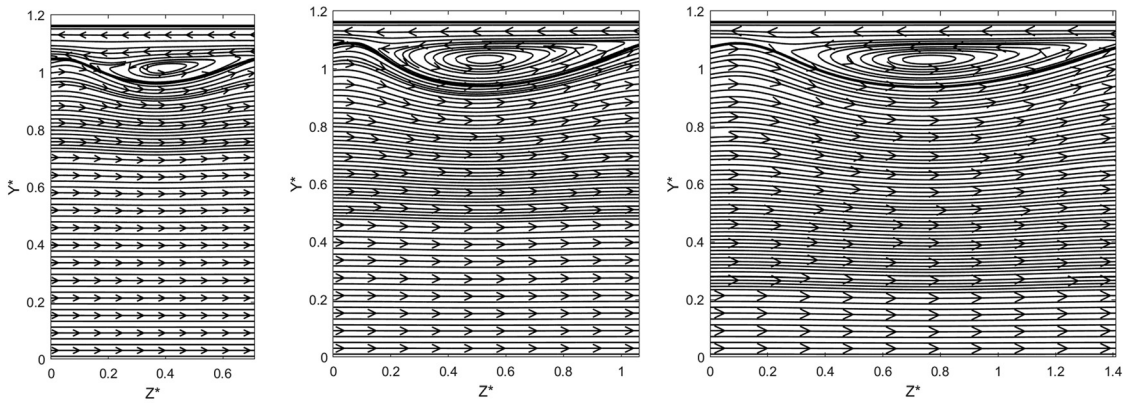

Fig. 11 Streamlines in a reference frame moving with the wave velocity: (*a*) $\lambda^* = 0.7$, (*b*) $\lambda^* = 1.1$, and (*c*) $\lambda^* = 1.4$

section length in the simulation length is taken longer than a certain value, multiple waves appear along the interface length in the simulation. Furthermore, because the simulation applies periodic boundary conditions, the largest wavelength cannot be above the pipe section length.

At a fully developed state, the oil core is balanced by pressure drop and two surface forces on the oil core: form drag and viscous shear force. In PCAF, the form drag in the axial direction is zero, and the viscous force is the only surface force. When waves have appeared at the interface, the pressure is redistributed on the oil core surface, creating a net force acting opposite to the streamwise direction. This force is so-called form drag, which can be calculated by integrating the pressure component in the streamwise direction along the interface. The magnitude of the form drag is related to the form of the wave. With increased wavelength, the form drag becomes more important in balancing the pressure drop. Besides, the shear stress force decreases slightly due to the larger and larger flow separation region near the interface.

To show the effect of the different wavelengths on the flow field, we probe the flow field at one fixed streamwise location. Figure 10 shows the interface location, wall pressure, maximum turbulent viscosity, and wall shear stress, as function of time. As the pressure gradient across the thickness of the water annulus is very small, the wall pressure also gives a very accurate representation of the pressure distribution near the interface. As can be seen, the saturated wave amplitude has increased with increasing wavelength. The flow field variation corresponds well with the wave amplitude. There is lower pressure at the back of the wave crest and higher pressure in front of the wave crest. At the wave trough, the pressure curve is rather flat. The wall shear stress increases significantly from PCAF to WCAF. Near the wave crest, the wall shear stress behaves like the pressure. For small waves, when the wavelength is $\lambda^* = 0.71$, both the pressure curve and the wall shear stress are more symmetric before and after the wave crest, which indicates a less tilted waveform. For $L^* = 0.29$, no waves occur, and PCAF does persist.

With increased wave amplitude, the peak value for the maximum turbulent viscosity increased slightly, while its lowest value decreased significantly for the cases with $L^* = 1.06$ and $L^* = 1.41$. When there is a wave crest passing by, the flow is locally laminar. The wave speed is 1.29 m/s for the case $L^* = 0.71$, 1.26 m/s for $L^* = 1.06$, and 1.24 m/s for $L^* = 1.41$.

The streamlines in the reference frame moving with the wave speed are shown for these three cases in Fig. 11: the recirculation zone increases with increasing wavelength.

5.4 Fully Developed Waves—Waveform. Figure 12 compares the wave amplitudes found for the different wavelengths in the numerical simulations and in the experiments. In each simulation, a single wavelength is simulated. The wave amplitude is taken as half the difference between the maximum and minimum thickness of the water annulus. These are the "single-wave simulations" in the figure. In addition, also a longer pipe section of 12 pipe diameters is simulated, which allows to track various waves in space and time. This is indicated as the "multiple-wave simulation" in the figure. In the experiments and in the multiple-wave simulation, the amplitude is determined as the average of the amplitudes of the waves that ended up in the ten intervals to determine the pdf of the wavelength distribution, as was explained in Sec. 5.2. Both in the simulations and in the experiments, the wave amplitude increases with increasing wavelength, up to a certain maximum level for the longest waves. As shown in Fig. 12, for the same wavelength in the experiments, the amplitude is larger in the bottom layer than in the top layer. This is related to the eccentricity of the oil core in the experiments, which gives a thicker water annulus at the bottom than at the top. The amplitudes obtained in the single-wave and multiple-wave simulations are very close. There is also a reasonably good agreement between the simulated wave amplitude and the measured amplitude; for example, the wavelength $\lambda^* = 1.5$ at a water holdup of 25% gives a wave amplitude that is 17% lower in the simulation than in the experiment (when comparing with the average amplitude of the waves in the top and bottom layers in the experiment). Obviously, as the simulation assumed axisymmetric flow, there is no difference between the top and bottom in the simulation.

The instantaneous waveform is shown in Fig. 13. The experimental wave and the numerical wave have a similar shape, in which the wave is slightly tilted, i.e., the wave slope in front of the wave crest is higher than behind the wave crest. This wave shape

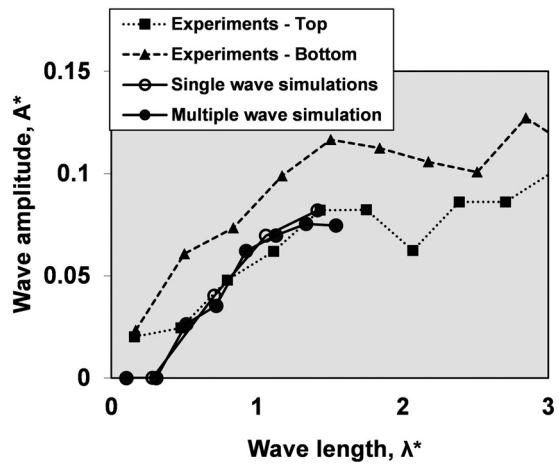

Fig. 12 Dimensionless wave amplitude (A^*) versus dimensionless wavelength (λ^*) as found in the simulations and experiments for 26% water holdup fraction

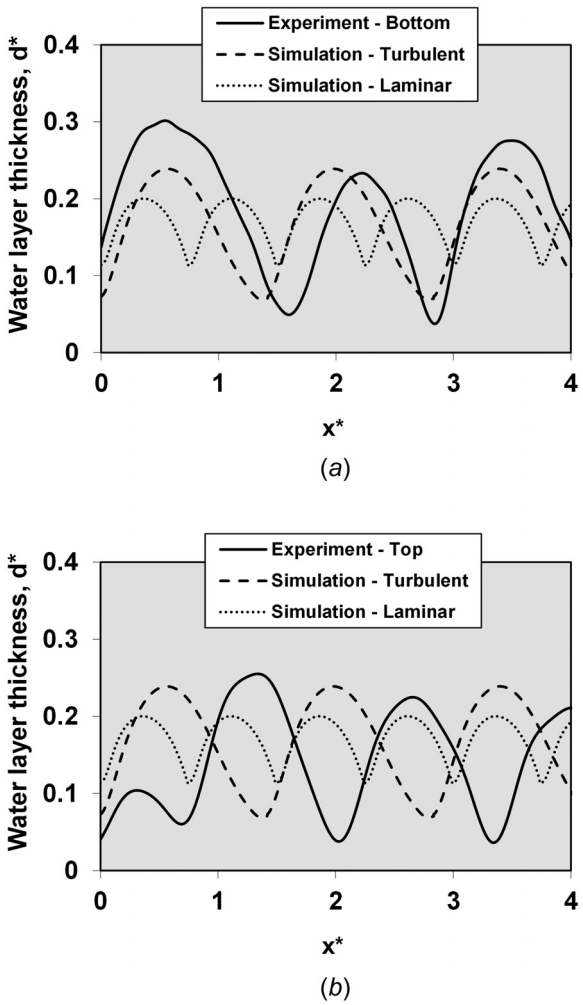

Fig. 13 Instantaneous waveform (for the dimensionless water layer thickness, d^*) in the experiments and simulations for a water holdup fraction of 26%: (*a*) top layer and (*b*) bottom layer. Note: the values as obtained at a fixed axial pipe location over time t^* are converted to the axial pipe coordinate x^*, through using the wave velocity.

corresponds to the flying core model proposed by Bai et al. [24] where the inertia effect is dominant. This is as expected since the flow in the water annulus is turbulent.

To compare the waveforms for turbulent and laminar flow conditions, the water viscosity is increased by a factor of ten in the simulation to replace the turbulent water annulus by a laminar one. The laminar waves are also included in Fig. 13. The waveform for the laminar condition is quite different from what is found for the turbulent condition; the wave in laminar flow is much shorter with a smaller amplitude, while the wave trough is flatter and the wave crest is more pointed. When the water viscosity is increased even further, the wave is broken and the wavy core-annular flow pattern is not stable anymore.

6 Conclusions

Numerical simulations are conducted for the wave initiation, growth, and saturation at the oil–water interface in core-annular flow, using the RANS approach with the Launder–Sharma low-Reynolds number $k-\varepsilon$ model. The focus is on conditions with a turbulent water annulus, but the laminar water annulus is considered as well. The simulation results are compared with lab measurements for fully developed flow with saturated waves.

The simulated growth rates for the laminar–laminar case are in close agreement with values obtained in the linear stability analysis by Li and Renardy [15]. The growth rate for the linear instability of different wavelengths (i.e., the wave stability curve) in the case of a turbulent water annulus can be obtained from 2D axisymmetric RANS simulations with the Launder–Sharma low-Reynolds number k–ε model. This also provides the most unstable wavelength for the turbulent water annulus. The maximum wave growth rate for a turbulent water annulus is significantly higher than for a laminar water annulus. Both in the simulations and in the experiments, the most unstable wavelength decreases with decreasing water holdup fraction (or decreasing watercut). The most unstable wavelength in the simulations is about 25% smaller than in the experiments.

The linear instability with exponential increase of the wave amplitude is followed by a nonlinear phase that ends in saturated waves in fully developed flow. The linear stage takes about four time units, and the nonlinear stage 16 time units (in which a time unit is the actual time nondimensionalized with the oil core radius and the mixture velocity). Both in the simulations and in the experiments for the fully developed saturated waves, the wave amplitude increases with increasing wavelength, up to a certain maximum level for the longest waves. The simulated amplitude of the different wavelengths is typically 17% lower than in the experiments.

The experiments and simulations are used to construct the probability density function of the wavelength distribution. If a relatively long pipe section is used in the simulations (i.e., 12 pipe diameters long, which is much longer than the most unstable wavelength), multiple wavelengths are predicted. The dominant wavelength in the spectrum (or pdf) is approximately the one that has the largest growth rate in the stability simulations. The pdfs for the wavelengths in the simulations and experiments are quite close to each other.

We apply a rather engineering simulation approach to the wave growth problem, based on just solving the flow equations with a turbulence model and tracking the wave evolution. The experiments only cover the fully developed saturated wave distribution, and not the controlled introduction and tracking of the linear and nonlinear growth of interfacial waves. However, the present engineering study can help to guide setting up a more in-depth theoretical study of these interesting but complex two-phase flow phenomena, involving the interplay between turbulence (in the annulus) and waves (at the liquid–liquid interface). For example, the results can be used to define relevant flow conditions for the eigenvalue analysis and for direct numerical simulations and large-eddy simulations and for controlled wave excitation in experiments.

Acknowledgment

The first author has received a grant from the China Scholarship Council (CSC). Thanks are also due to the Netherlands Foundation of Scientific Research (NWO) for supplying the computer time.

Funding Data

- China Scholarship Council (CSC) (Funder ID: 10.13039/501100004543).

Data Availability Statement

The datasets generated and supporting the findings of this article are obtainable from the corresponding author upon reasonable request.

Nomenclature

A = wave amplitude, m
e = core eccentricity
$F_{\sigma,i}$ = specific interfacial tension force, N/m^3
g = gravitational acceleration, m/s^2
h = holdup ratio
i = subscript referring to spatial coordinate direction
k = turbulent kinetic energy, m^2/s^2

k^* = dimensionless wave growth rate
L = pipe section length considered in the simulation
o = subscript referring to the oil phase
Q = volumetric flow rate, m^3/s
r = radius, m
R_c = core radius, m
t = time, s
u_i = velocity component, m/s
U_c = streamwise velocity at the pipe center, m/s
V = volume, m^3
w = subscript referring to the water phase
WC = watercut
x = coordinate along the pipe axis, m
y = pipe coordinate perpendicular to the pipe axis, m
z = pipe coordinate perpendicular to the pipe axis, m
$*$ = superscript denoting dimensionless quantity
γ = wave number, m^{-1}
ε = turbulence dissipation rate, m^4/s^3
ϑ = pipe inclination angle with respect to the horizontal, deg
λ = wavelength, m
μ = dynamic viscosity, Pa·s
ν = kinematic viscosity, m^2/s
ν_t = turbulent viscosity, m^2/s
ρ = density, kg/m^3
σ = interfacial tension, N/m

References

[1] Joseph, D. D., Bai, R., Chen, K. P., and Renardy, Y. Y., 1997, "Core-Annular Flows," Annu. Rev. Fluid Mech., **29**(1), pp. 65–90.
[2] Chen, K., Bai, R., and Joseph, D. D., 1990, "Lubricated Pipelining. Part 3 Stability of Core-Annular Flow in Vertical Pipes," J. Fluid Mech., **214**, pp. 251–286.
[3] Yih, C. S., 1967, "Instability Due to Viscosity Stratification," J. Fluid Mech., **27**(2), pp. 337–352.
[4] Hooper, A. P., 1985, "Long-Wave Instability at the Interface Between Two Viscous Fluids: Thin Layer Effects," Phys. Fluids, **28**(6), pp. 1613–1618.
[5] Hickox, C. E., 1971, "Instability Due to Viscosity and Density Stratification in Axisymmetric Pipe Flow," Phys. Fluids, **14**(2), pp. 251–262.
[6] Ooms, G., 1971, "Fluid-Mechanical Studies on Core-Annular Flow," Ph.D. thesis, Delft University of Technology, Delft, The Netherlands.
[7] Hooper, A. P., and Boyd, W. G. C., 1983, "Shear-Flow Instability at the Interface Between Two Viscous Fluids," J. Fluid Mech., **128**, pp. 507–528.
[8] Preziosi, L., Chen, K., and Joseph, D. D., 1989, "Lubricated Pipelining: Stability of Core-Annular Flow," J. Fluid Mech., **201**, pp. 323–356.
[9] Charles, M. E., Govier, G. W., and Hodgson, G. W., 1961, "The Horizontal Pipeline Flow of Equal Density Oil-Water Mixtures," Can. J. Chem. Eng., **39**(1), pp. 27–36.
[10] Hu, H. H., and Joseph, D. D., 1989, "Lubricated Pipelining: Stability of Core-Annular Flow. Part 2," J. Fluid Mech., **205**, pp. 359–396.
[11] Bai, R., Chen, K., and Joseph, D. D., 1992, "Lubricated Pipelining: Stability of Core-Annular Flow. Part 5," J. Fluid. Mech., **240**, pp. 97–132.
[12] Miesen, R., Beijnon, G., Duijvestijn, P. E. M., Oliemans, R. V. A., and Verheggen, T., 1992, "Interfacial Waves in Core-Annular Flow," J. Fluid Mech., **238**, pp. 97–117.
[13] Boomkamp, P. A. M., and Miesen, R. H. M., 1996, "Classification of Instabilities in Parallel Two-Phase Flow," Int. J. Multiphase Flow, **22**, pp. 67–88.
[14] Papageorgiou, D. T., Maldarelli, C., and Rumschitzki, D. S., 1990, "Nonlinear Interfacial Stability of Core-Annular Film Flows," Phys. Fluids A: Fluid Dyn., **2**, pp. 340–352.
[15] Li, J., and Renardy, Y., 1999, "Direct Simulation of Unsteady Axisymmetric Core–Annular Flow With High Viscosity Ratio," J. Fluid Mech., **391**, pp. 123–149.
[16] Beerens, J. C., Ooms, G., Pourquié, M. J. B. M., and Westerweel, J., 2014, "A Comparison Between Numerical Predictions and Theoretical and Experimental Results for Laminar Core-Annular Flow," AIChE J., **60**(8), pp. 3046–3056.
[17] Kuru, W. C., Sangalli, M., Uphold, D. D., and McCready, M. J., 1995, "Linear Stability of Stratified Channel Flow," Int. J. Multiphase Flow, **21**(5), pp. 733–753.
[18] Náraigh, L. Ó., Spelt, P. D. M., Matar, O. K., and Zaki, T. A., 2011, "Interfacial Instability in Turbulent Flow Over a Liquid Film in a Channel," Int. J. Multiphase Flow, **37**(7), pp. 812–830.
[19] Li, H., Pourquié, M. J. B. M., Ooms, G., and Henkes, R. A. W. M., 2021, "Simulation of Turbulent Horizontal Oil-Water Core-Annular Flow With a Low-Reynolds Number k-ϵ Model," Int. J. Multiphase Flow, **142**, p. 103744.
[20] Li, H., Pourquié, M. J. B. M., Ooms, G., and Henkes, R. A. W. M., 2022, "Simulation of a Turbulent Annulus With Interfacial Waves in Core-Annular Pipe Flow," Int. J. Multiphase Flow, **154**, p. 104152.
[21] Vrijlandt, D. W. S., 2020, "Visualisation and Quantification of Oil-Water Core-Annular Flow," Master thesis, Repository of Delft University of Technology, Delft, The Netherlands.
[22] Launder, B. E., and Sharma, B. T., 1974, "Application of the Energy Dissipation Model of Turbulence to the Calculation of Flow Near a Spinning Disc," Lett. Heat Mass Transfer, **1**(2), pp. 131–137.
[23] Yamamoto, T., Okano, Y., and Dost, S., 2017, "Validation of the S-CLSVOF Method With the Density-Scaled Balanced Continuum Surface Force Model in Multiphase Systems Coupled With Thermocapillary Flows," Int. J. Numer. Methods Fluids, **83**(3), pp. 223–244.
[24] Bai, R., Kelkar, K., and Joseph, D. D., 1996, "Direct Simulation of Interfacial Waves in a High-Viscosity-Ratio and Axisymmetric Core-Annular Flow," J. Fluid Mech., **327**, pp. 1–34.